Investigations of ambient light emission at deep-sea hydrothermal vents

Sheri N. White and Alan D. Chave

Department of Applied Ocean Physics and Engineering, Woods Hole Oceanographic Institution,
Woods Hole Massachusetts, USA

George T. Reynolds

Department of Physics, Princeton University, Princeton, New Jersey, USA

[1]   The Ambient Light Imaging and Spectral System (ALISS) was used to image ambient light from black smokers, flange pools, and a beehive on the East Pacific Rise and the Juan de Fuca Ridge. ALISS is a low-light digital camera with custom-designed optics. A set of nine lenses, each covered by an individual band-pass filter, allows an identical scene to be imaged simultaneously in nine wavelength bands spanning the range of 400–1000 nm. Thus information about both the location and the spectral character of emitting regions is obtained. The primary source of light at deep-sea vents is thermal radiation due to the high temperature of the hydrothermal fluid. This thermal light peaks in the infrared with a tail that extends into the visible. Data suggest that flange pools have an emissivity of ~0.9 and black smoker fluids have an emissivity of ~0.3. Thermal radiation dominates at wavelengths >700 nm (with a photon flux that increases from $\sim10^6$ photon cm^{-2} s^{-1} sr^{-1} at 700 nm to $\sim10^{10}$ photon cm^{-2} s^{-1} sr^{-1} at 1000 nm). Temporally variable light is observed in the 400–600 nm region of the spectrum that is orders of magnitude greater than predicted for a thermal source (i.e., on the order of 10^4 rather than $10^{-2}–10^3$ photons cm^{-2} s^{-1} sr^{-1}). This light is probably caused by mechanisms associated with turbulence, mixing and precipitation, such as vapor bubble luminescence, chemiluminescence, crystalloluminescence and triboluminescence. While biological responses to vent light are not yet known, observed light levels are too low to support obligate photosynthesis.   INDEX TERMS: 4552 Oceanography: Physical: Ocean optics, 3035 Marine Geology and Geophysics: Midocean ridge processes, 3094 Marine Geology and Geophysics: Instruments and techniques; KEYWORDS: Hydrothermal Vents, Ocean Optics

1. Introduction

[2]   Light has long been known to exist in the deep ocean in the form of bioluminescence (light emission from organisms) [e.g., *Bradner et al.*, 1987] and Cerenkov radiation (light emission from radioactive decay particles traveling faster than the speed of light in the medium) [*Belcher*, 1953]. While bioluminescence is visible to the unaided eye, Cerenkov radiation produces subscotopic background radiation in the ocean (~150 photons cm^{-2} s^{-1} emitted into a half-space in the 300–630 nm range) [*Roberts*, 1979]. Recently, it was discovered that high-temperature hydrothermal vents are also a source of light in the deep ocean. This brings up interesting questions regarding the sources of this light and the possible effect on the surrounding biological communities: What is the sources (or sources) of vent light and what does it tell us about physical and chemical processes occurring there? Can organisms living in the vent environment detect this light? If so, how is this information used?

[3]   The idea that hydrothermal vents emit visible light was first suggested by *Van Dover et al.* [1989] following the discovery of a novel photoreceptor on the dorsal side of the Mid-Atlantic Ridge vent shrimp *Rimicaris exoculata*. This large organ, which contains the photopigment rhodopsin, does not possess imaging capabilities, but it is uniquely designed to detect very low levels of light [*O'Neill et al.*, 1995]. *Pelli and Chamberlain* [1989] calculated

that the thermal (blackbody) radiation due to the high vent temperatures ($\sim350°C$) was significant enough to be detected by *R. exoculata* but not by humans. The existence of vent light was confirmed in 1988 when ambient light from a high-temperature black smoker on the Juan de Fuca Ridge was imaged with a charge-coupled device (CCD) camera [*Smith and Delaney*, 1989; *Van Dover et al.*, 1994]. Subsequent investigations of vent light (at Snake Pit on the Mid-Atlantic Ridge and Hole-to-Hell on the East Pacific Rise) using a simple nonimaging photometer called Optical Properties Underwater Sensor (OPUS) focused on the red to near-infrared region of the spectrum (700–1000 nm) where thermal radiation was suspected to be strongest [*Van Dover et al.*, 1996]. These studies found temporal variability and excess flux over that expected for a blackbody, both of which suggest sources other than thermal radiation. Later investigations with OPUS (in the 9°N area of the East Pacific Rise) revealed that visible light (in the 400–750 nm range) was also present that could not be explained by thermal radiation alone [*White et al.*, 1996].

[4]   Upon exiting a hydrothermal vent orifice, the high-temperature fluid immediately mixes with cold ($\sim2°C$) ambient seawater, creating a rising plume of cooling hydrothermal fluid in which metallic minerals precipitate. Thermal radiation is expected to be greatest at the orifice where the temperature is highest. However, other mechanisms of light emission may occur in other parts of the plume away from the orifice and are expected to have unique spectral characteristics. OPUS (or any other nonimaging spectrometer) lacks the ability to image vent light, thus limiting its ability to adequately characterize vent light. A new instrument, Ambient
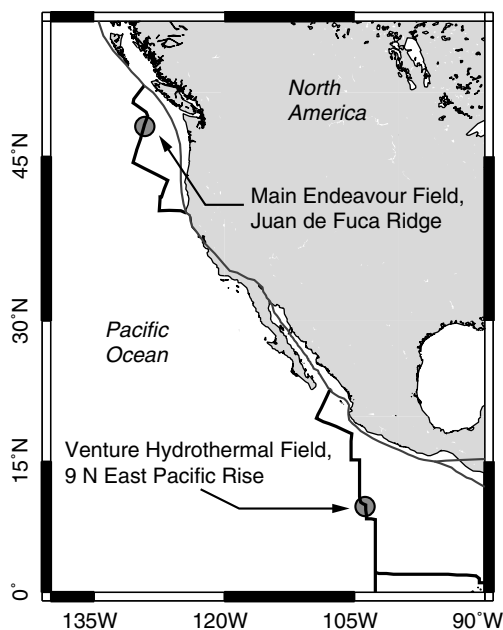
Figure 1. ALISS was deployed at two sites in the Pacific: the Venture Hydrothermal Field at ~2500 m depth at 9°N on the East Pacific Rise and the Main Endeavour Field at ~2200 m depth on the Endeavour Segment of the Juan de Fuca Ridge (47°57′N). Plate boundaries are indicated by dark shaded lines, and vent site locations are indicated by shaded circles.

Light Imaging and Spectral System (ALISS), was developed to overcome this deficiency. ALISS is a low-light CCD camera with custom-designed optics which allow it to image a scene simultaneously in nine wavelength bands. By using long exposure times and image processing techniques, even very low levels of light (on the order of 10^3 photons cm^{-2} s^{-1} per unit solid angle at a distance of 50 cm in water) can be detected and analyzed, and the emitting region can be localized.

[5] *White et al.* [2000] presented preliminary ALISS data from the Main Endeavour Field of the Juan de Fuca Ridge. This paper discusses a broader set of data collected from two deployments of the ALISS camera system in the Pacific and goes a step further in processing the data to translate the count rates detected at the ALISS camera to photon fluxes (in photons cm^{-2} s^{-1} sr^{-1}) at the vent orifice. Rough spectra obtained from flange pools, black smoker chimneys, and a beehive vent suggest that whereas thermal radiation is ubiquitous at high-temperature vents, temporally varying, visible radiation (400–700 nm) is also present and cannot be explained by thermal radiation alone. While a mechanism for this visible light has yet to be determined unequivocally, one or more of a number of sources (e.g., chemiluminescence, vapor bubble luminescence, triboluminescence, and crystalloluminescence) appear to be candidates.

2. Field Sites

[6] ALISS was deployed on two *Alvin* dive cruises to hydrothermal fields in the eastern Pacific: a November–December 1997 cruise to the Venture Hydrothermal Field on the East Pacific Rise (EPR), and a June–July 1998 cruise to the Main Endeavour Field of the Juan de Fuca Ridge. The Venture Hydrothermal Field (Figure 1) is located within the axial summit caldera (ASC) of the EPR from 9°30′N to 9°54′N and consists of a number of high-temperature (>350°C) black smokers as well as beehive structures (see *Tivey and Delaney* [1995] for descriptions), areas of diffuse low-temperature flow and associated biological communities [*Haymon et al.*, 1991].

Beehive structures (or "diffusers") are high-porosity bulbous features through which hydrothermal fluids percolate and emanate as clear fluids cooler than 350°C [*Tivey and Delaney*, 1995].

[7] Hydrothermal venting on the Endeavour Segment of the Juan de Fuca Ridge (Figure 1) is located along the western wall of the rift valley at 47°57′N, 129°06′W and a depth of 2200 to 2220 m [*Crane et al.*, 1985; *Tivey and Delaney*, 1986]. The Main Endeavour Field (described in detail by *Delaney et al.* [1992]) consists of a number of large (20 m × 25 m × 20 m) sulfide structures covering an area 300 m × 400 m. In addition to black smokers, flange pools (high-temperature fluids trapped beneath sulfide-sulfate-silica flanges) are also found on the Endeavour segment. Fluids pooled beneath these flanges are stably stratified, forming a sharp interface with the ambient (~2°C) seawater through which minimal mixing occurs [*Delaney et al.*, 1992].

3. Instrumentation

3.1. Camera Design

[8] ALISS is a Princeton Instruments PentaMAX camera with a thermoelectrically cooled SITe 1024×1024 pixel CCD chip (Figure 2a). CCD's are small, linear, low-power devices with excellent sensitivity over wide ranges of wavelength and intensity. They are inherently integrating devices that can image very faint objects by using long exposure times to build up charge in the CCD pixels.
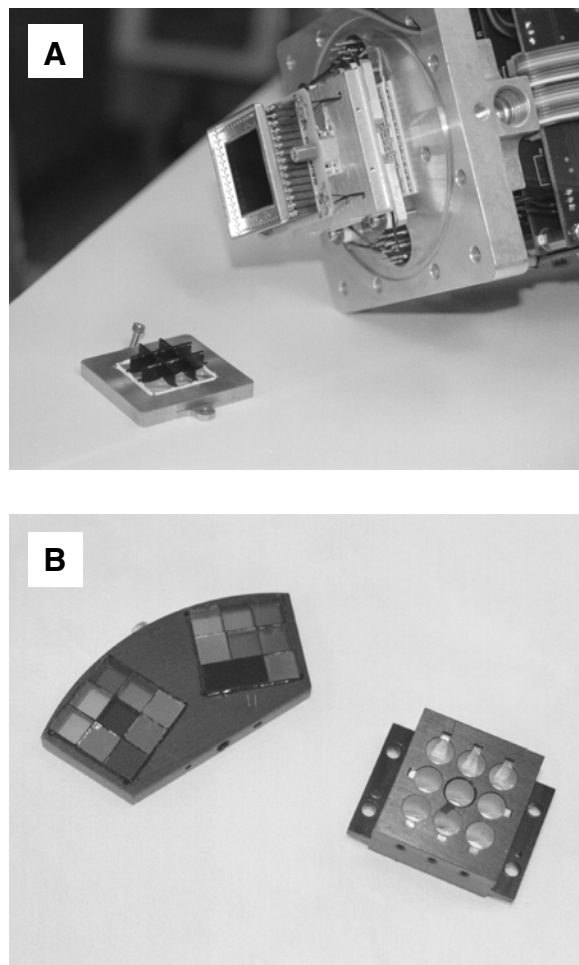

Figure 2. ALISS optical assembly. (a) Field flattener lenses with baffles (front left) prior to being mounted over the CCD chip. (b) Filter arrays (left) and optic block (containing the nine triplet lenses).

Digital images captured by the CCD can be processed and analyzed by computer to extract data such as variations or low intensity levels that are imperceptible to the unaided eye. ALISS uses an AR-coated, back-illuminated, multipinned phase (MPP) CCD chip with a peak quantum efficiency of 80% at 640 nm, which decreases to ~64% and 20% at 400 nm and 1000 nm, respectively. In order to simultaneously image the same object in a number of different wavelength bands, the 1024×1024 pixel CCD plane is divided into nine ~300×300 pixel tiles by a set of baffles and field-flattening lenses (Figure 2a). An optic block positioned over the CCD (Figure 2B) contains nine triplet lenses which focus the same scene onto each tile. A nine-filter array placed in front of the lens assembly covers each lens with an individual interference band-pass filter. ALISS contains two such filter arrays (Figure 2b) so that images can be obtained in 18 different wavelength bands on each *Alvin* dive. Eleven of the filters are ~100 nm in bandwidth, six are ~50 nm in bandwidth, and one is 10 nm in bandwidth (centered on 589 nm). The filters overlap to provide complete coverage of the spectrum from 400 to 1000 nm and are IR blocked above 1200 nm. The camera is housed in a titanium pressure case with an optical window that is a 2-inch-thick, $62°$ sector of a dome with a 4-inch internal radius. The optical system (field flatteners, lenses, filters, and optical window) has a field of view of 15×15 cm at a distance of 50 cm.

3.2. Noise

[9] ALISS data are subject to noise inherent to any electronic camera system. CCD noise sources include thermal noise associated with dark charge, photon noise associated with the signal, and readout noise associated with the electronics. ALISS's CCD is maintained at $-50°C$ by a thermoelectric cooler to limit thermally produced charges (dark charge) that build up over time. The dark noise of an ALISS image is $\sim 1-2$ electrons pixel^{-1}. The build up of signal on a CCD chip by incoming photons can be described as a Poisson process, and as such, the variance is equal to the mean of the signal. The greater the incoming signal, the higher the signal-to-noise ratio. Readout noise, unlike photon and thermal noise which originate in the imaging area of the CCD chip, is generated in the output preamplifier. The readout noise of the ALISS camera is 12 electrons pixel^{-1}. The combination of dark noise and readout noise determines the effective detection limit of the camera.

3.3. Calibration

[10] ALISS was calibrated as a complete optical system (i.e., in its pressure case) prior to the 1997 EPR cruise using the Palomar Observatory Group's Quantum Efficiency (QE) Test System at the California Institute of Technology. The QE test device consists of an Oriel 66002 deuterium lamp, a mono-chrometer, and an NBS-calibrated photodiode [*Behr*, 1996]. Measurements were made every 10 nm from 400 to 1040 nm, providing 5 to 10 calibration points per filter. Dividing the count rate measured by ALISS by the photon flux incident on ALISS's pressure window (determined from the photodiode) yields the effective aperture of the ALISS camera system. Effective aperture includes the entrance pupil of the lens, transmission through the optical assembly (pressure window, filters, and lenses), and the QE of the CCD chip. The camera was calibrated in air; to account for the smaller entrance pupil when imaging in water, the measured effective aperture was divided by the square of the index of refraction of water ($1.33^2 = 1.77$).

3.4. Operations

[11] ALISS was mounted on a frame in the *Alvin* science basket such that the camera could be raised and tilted with two hydraulic rams and panned left and right with the *Alvin* manipulator. To image hydrothermal vents, the submersible was stably positioned so that the ALISS pressure window was 50 cm from the vent (the lens-object distance of the camera) as indicated by
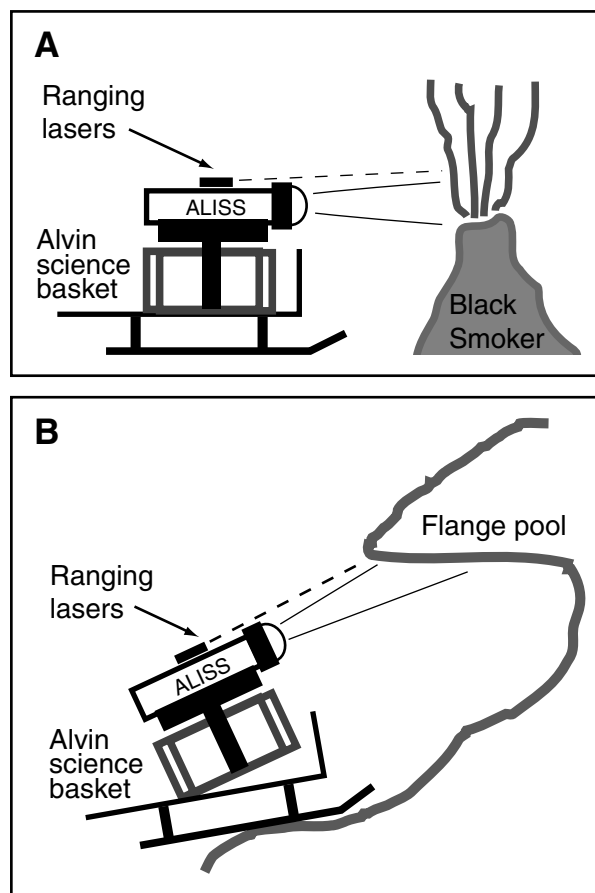

Figure 3. Schematic showing how ALISS is positioned at (a) black smokers and (b) flanges pools. Ranging lasers cross at 50 cm from the optical window (the focal point of the ALISS camera).

two lasers aligned to cross at that distance (Figure 3). Images of ambient vent light (5-min exposures) were made with *Alvin's* external lights and lasers secured and the viewports blocked to prevent light contamination from the submersible. Images of the vent illuminated by *Alvin* lights were obtained to compare the location of ambient light emission to the location of the sulfide structure and plume. Additional images were also collected during the dives to correct for systematic errors during image processing (see section 4).

4. Data Analysis

4.1. Image Processing

[12] ALISS images were processed using two image processing packages: Image Reduction and Analysis Facility (IRAF) distributed by the National Optical Astronomy Observatories, and Interactive Data Language (IDL) distributed by Research Systems, Inc. A number of corrections must be made to remove additive and multiplicative systematic errors from the images (discussed in detail by *Tyson* [1986, 1990]) to perform accurate photometry. The image reduction steps are as follows:

1. Remove DC bias level. Determined from a 20-column overscan strip (20 more columns are read than exist on the CCD array).

2. Subtract bias structure. A fixed pattern associated with the CCD; obtained by averaging together a number of zero-second exposures.
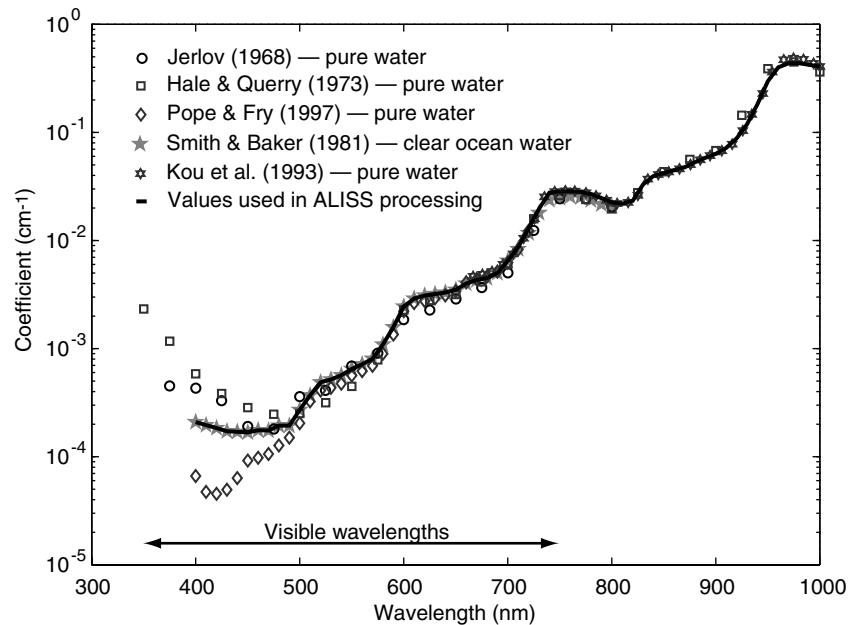
Figure 4. Attenuation coefficients of water and seawater. The literature values [*Hale and Querry*, 1973; *Jerlov*, 1968; *Kou et al.*, 1993; *Pope and Fry*, 1997; *Smith and Baker*, 1981] are consistent at long wavelengths and show variation at short wavelengths. The dark line indicates the values used to process ALISS data (from *Smith and Baker*, 1981; *Kou et al.* [1993], and modified for temperature as described by *Pegau et al.* [1997]). The visible region of the spectrum is from 350 to 750 nm.

3. Subtract dark charge. Thermal signal built up on the CCD without external illumination, obtained by averaging together a number of closed-shutter, 5-min exposures.

4. Median average multiple vent images to reduce noise. The standard deviation (σ) for one pixel varied from ~0.01 in the background (~0.01 counts s^{-1} signal) to ~0.7 in the source area (maximum signal of ~1–3 counts s^{-1})

5. Divide by flat field to correct for pixel-to-pixel variations. A flat-field image is made by imaging an evenly illuminated surface; these images were obtained on deck prior to each dive. During the image processing of the vent images the flat-field correction (dividing the vent image by the flat field) was made on a tile-by-tile basis.

[13] Once the vent images were processed as described above, a source mask and complementary background mask were created using the channel with the highest signal-to-noise ratio (typically, the 870-nm filter) to isolate the area of light emission from the background. The same mask was applied to all 18 channels and count rates (minus the background levels scaled to the number of pixels in the source mask) were calculated for all filters. These values were divided by the source area giving the detected count rate at the ALISS CCD for each filter in counts cm^{-2} s^{-1}. Analyses of specific parts of the plume were performed by limiting the source mask to a certain region, or to intensities within a specific range (i.e., from 0 to 100% of the intensity values measured). The light observed in the 870-nm channel was assumed to be dominated by thermal radiation. Thus variation in light intensity in this band can be used to indicate variation in temperature. In analyzing the spectrum of black smoker light we isolated portions of the source area into four quartiles based on intensity (or temperature): the 75–100 percentile region being the brightest/hottest quartile of the pixels and the 0–25 percentile region being the darkest/coolest quartile of the pixels.

4.2. Attenuation

[14] Since light emitted at hydrothermal vents travels through 50 cm of water before reaching the ALISS camera, attenuation of light in water is an important optical property that must be included when analyzing data. Attenuation due to either absorption or scattering is exponential with distance and is characterized by a wavelength-dependent attenuation coefficient. This wavelength dependence confines much of ocean optical research to the visible region of the spectrum where light is attenuated the least. A summary of attenuation coefficients found in the literature is shown in Figure 4. Shoulders and peaks are present in the visible and near infrared regions of the attenuation spectrum at overtones of the O-H vibrational frequencies.

[15] A number of scientists have experimentally determined the attenuation coefficients of both pure water and seawater [e.g., *Curcio and Petty*, 1951; *Hale and Querry*, 1973; *Pope and Fry*, 1997; *Smith and Baker*, 1981; *Sullivan*, 1963]. In most cases, the water used in these experiments was filtered to remove particulate matter which causes scattering. An attempt was made to measure the attenuation of water in the vent environment using the ALISS camera. This proved to be difficult due to the large bandwidth of the filters and sidelobe leakage. Because of the rapid change in attenuation with wavelength, a resolution of 10 nm is preferred, which cannot be obtained by ALISS's 50- and 100-nm bandwidth filters. Therefore the attenuation coefficients used for analyses of ALISS data are taken from *Smith and Baker* [1981] (seawater at 20°C) for wavelengths <700 nm and *Kou et al.* [1993] (pure water at 22°C) for the 700–1000 nm range. These values were modified to account for the differences in temperature and salinity as described by *Pegau et al.* [1997]. *Smith and Baker*'s [1981] experiments used filtered seawater to remove the effects of scattering. Rayleigh scattering by particles smaller than the wavelength of light selectively scatter shorter wavelengths more than long wavelengths (i.e., the visible region is more likely to be affected by scattering than the infrared). Given the presence of particulate matter in the vent environment, the attenuation is probably higher than the literature values. However, given the low coefficient values in the visible region (10^{-3} to 10^{-4} cm^{-1}) and the distance

through which ALISS is imaging (50 cm), this has very little effect. The attenuation curve used in the ALISS calculations is shown by the solid line in Figure 4.

4.3. Inversion Method

[16] The photon flux from a vent is the number of photons emitted at the source per unit area per unit time per unit solid angle. This photon flux is attenuated as it travels through seawater and the ALISS optics, and is integrated over each filter, resulting in a count rate for each channel:

$$\text{Flux}_{\text{vent}}\Omega e^{-\kappa x}T_{\text{ALISS}}\text{QE} = \text{CR}_{\text{ALISS}}\text{Gain}, \qquad (1)$$

where $\text{Flux}_{\text{vent}}$ is the photon flux at the vent in photons $\text{cm}^{-2}\ \text{s}^{-1}\ \text{sr}^{-1}$, Ω is the solid angle subtended by the camera (i.e., the area of the entrance pupil of the camera divided by the square of the camera-vent distance, x^2) in steradians and is 4.5×10^{-5} sr for each lens at 50 cm, κ is the attenuation coefficient of seawater in cm^{-1} (Figure 4), T_{ALISS} is the transmission through the ALISS optics, QE is the quantum efficiency of the CCD (i.e., the number of electrons produced by an incident photon), CR_{ALISS} is the count rate measured by ALISS in counts $\text{cm}^{-2}\ \text{s}^{-1}$, and the gain of the camera is 6.1 electrons count^{-1}. The effective aperture (A_{eff}) of the camera (determined by calibration) includes the entrance pupil, the transmission through the ALISS optics (pressure window, filters, and lenses), and the QE of the CCD. Thus (1) can be written as

$$\text{Flux}_{\text{vent}}e^{-\kappa x}(A_{\text{eff}}/x^2) = \text{CR}_{\text{ALISS}}\text{Gain}. \qquad (2)$$

Our goal is to backward continue the ALISS data from the CCD (hereinafter referred to as "count rate") to the vent to determine the photon flux at the vent orifice (hereinafter referred to as simply "photon flux"). Backward continuation becomes unstable due to the exponential factor in the equation; small errors are greatly expanded at long wavelengths during backward continuation. Additionally, the light transmitted through a filter is not entirely confined to the specified passband due to sidelobe leakage. For example, the 450-nm filter has a transmission of ~75% in the passband (400–500 nm) while outside of the passband the transmission is reduced by 4 orders of magnitude (Figure 5a). When observing a 350°C blackbody radiator, the photon flux at long wavelengths (>700 nm) is more than 4 orders of magnitude greater than the flux at 450 nm. Thus leakage occurs because the long-wavelength emission cannot be suppressed to insignificant levels with respect to the short-wavelength emission (Figure 5b). The attenuation coefficient is wavelength-dependent and increases significantly from 450 to 950 nm. Without being able to separate the flux by wavelength, an appropriate attenuation value cannot be determined to backward continue the data on a filter by filter basis (the light emission and attenuation coefficients can vary greatly over the 100-nm filter bandwidth). This problem affects all filters to some extent. Therefore an inversion routine is necessary to translate the ALISS data from integrated count rates at the CCD to continuous photon flux at the vent.

[17] Inversion of data does not result in a unique solution. A number of possible models can fit the observed data to a given degree of tolerance. Therefore some method must be used to restrict the outcome to a range of models that have physical significance or are based on a priori information or constraints. This approach originated with *Tikhonov* [1963a, 1963b] (see also *Franklin* [1970] for a more general treatment) and has been adopted widely for geophysical inversion. For example, *Constable et al.* [1987] and *Smith and Booker* [1988] applied
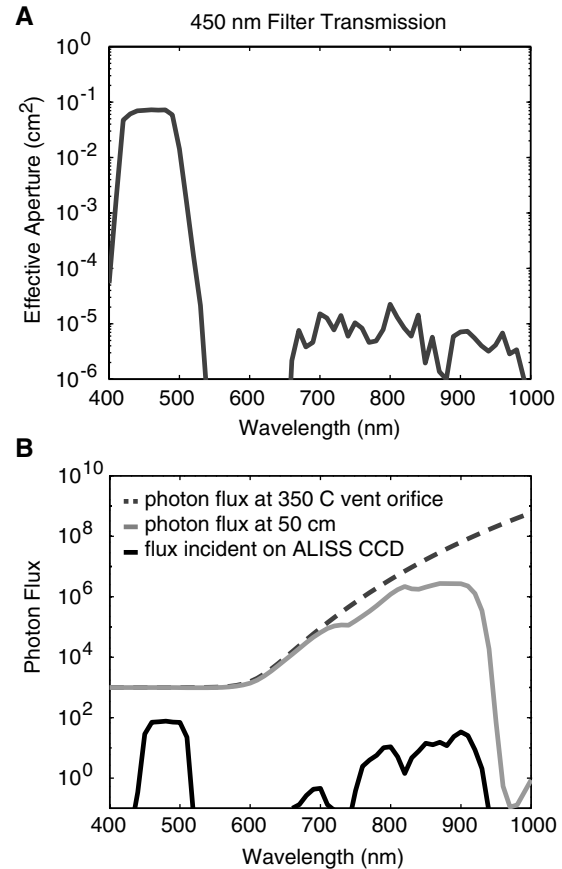

Figure 5. The 450-nm filter curve and blackbody transmission through filter. (a) Effective aperture of ALISS through the 450-nm filter determined from calibration. (b) Synthetic photon flux (350°C blackbody with 10^3 photons $\text{cm}^{-2}\ \text{s}^{-1}\ \text{sr}^{-1}$ added at all wavelengths) shown by the dashed line. After passing through 50 cm of water, the photon flux is attenuated as shown by the shaded line. Light that passes through the ALISS optics is shown by the solid line. Significant leakage occurs at long wavelengths (750–950 nm).

regularization to the inversion of magnetotelluric data by seeking the smoothest model consistent with a given set of data.

[18] Before discussing the inversion, we will describe the simpler case of the forward model:

$$D = F[m], \qquad (3)$$

where d is a set of M data points, F is the forward functional (approximated as an $M \times N$ matrix), and m is a model that is N long. In our case, m is the photon flux at the vent ($\text{Flux}_{\text{vent}}$) (in 10-nm increments from 400 to 1040 nm); F describes how the photon flux is attenuated through seawater and the ALISS optics ($e^{-\kappa x}$ (A_{eff}/x^2)) every 10 nm from 400 to 1040 nm; and d is the resulting data ($\text{CR}_{\text{ALISS}}\text{Gain}$) summed over each filter.

[19] We define a roughness parameter as the integrated square of the first derivative with respect to wavelength:

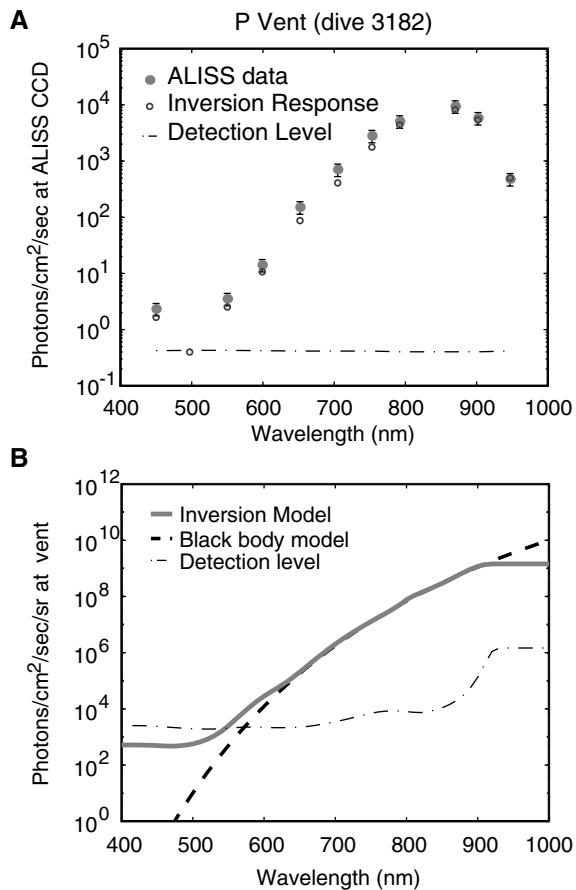$$R_1 = \int (dm/d\lambda)^2 d\lambda, \qquad (4)$$

A

B

Figure 6. Inversion of ALISS data from P Vent (9°N EPR). (a) ALISS data (shaded dots) with 25% uncertainty error bars are compared to the response of the inversion model (solid circles) shown in Figure 6b. The high data value from the 450-nm filter with respect to the 500-nm filter is due to long-wavelength leakage (see Figure 5). (b) Inversion of the ALISS data (shaded line) is compared to a 340°C blackbody with an emissivity of 0.3. The inversion model tends to flatten at either end (400–500 and 900–1000 nm) and cannot resolve values below the detection level of the ALISS camera (dash-dotted line).

where R_1 is the first derivative roughness, m is the model, and λ is wavelength. The inversion algorithm uses a series of iterations to search for the smoothest possible model (m) that fits the data (d) with uncertainty (σ) to within a chosen misfit (X^2). The misfit is expressed as

$$x^2 = \|Wd - WF[m]\|^2, \quad (5)$$

where W is a diagonal $M \times M$ weight matrix

$$W = \mathrm{diag}\{1/\sigma_1, 1/\sigma_2, \ldots, 1/\sigma_M,\} \quad (6)$$

and parallels denote the Euclidean norm. For ALISS data the uncertainty (σ) in the data is due to noise in the camera system and uncertainty in the actual camera-vent distance. Camera noise is dominant at the shorter wavelengths and is ~25% of the signal. At long wavelengths, uncertainty in the camera-vent distance is dominant. At ~870 nm, where the highest signal is observed, a 5–10 cm error in distance results in a 22–49% error in count rate. Therefore we define an uncertainty of 25% for all data points. Because this uncertainty cannot be better constrained, the misfit that can be achieved is limited.

[20] It may seem odd to seek the smoothest model, when it is possible for sharp discontinuities to occur in the data (e.g., emission bands). However, because of the width of the ALISS filters (nominally 100 nm), the camera is not capable of resolving such peaks. Thus the smoothed model is able to show regions of excess emission that can be detected given the resolution of the camera.

[21] An example of ALISS data and an inversion model is shown in Figure 6. ALISS data (i.e., the count rate detected by the camera at a distance of 50 cm from the vent) from P vent (9°N EPR) are plotted as shaded dots in Figure 6a. The count rates tend to increase with increasing wavelength as expected for a thermal source. The decrease in count rate above 870 nm is due to the increasing significance of attenuation in that region (see Figure 4). The inversion technique described above was used to determine a photon flux at the vent from the count rates recorded by the ALISS camera. The inversion model (photon flux) is plotted as a solid line in Figure 6b and is compared to a theoretical thermal source (340°C blackbody of emissivity of 0.3). Flattening occurs at the extreme ends of the model due to the lack of constraints outside of the 400–1040 nm region and the restriction on the inversion method to generate the smoothest (i.e., flattest) possible model. The center portion of the model corresponds well to a blackbody flux. The response of the inversion model (i.e., the predicted ALISS count rate resulting from running the inversion model
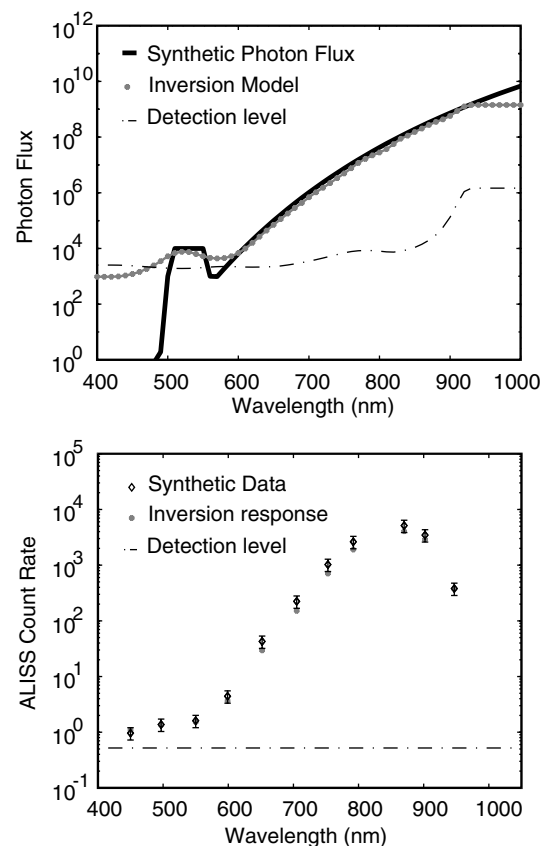

Figure 7. Inversion of synthetic data. (a) A synthetic flux (330°C blackbody with an excess flux of 10^4 photons cm^{-2} s^{-1} sr^{-1} in 500–550 nm region) run through the forward functional to generate synthetic ALISS data (shown in Figure 7b with 25% error bars). The data were then inverted (shaded dotted line) and compared to the original synthetic flux (solid line) (Figure 7a). The inversion successfully returns the blackbody curve, and the excess flux in the visible region is well approximated by the inversion program. (b) Comparison of the synthetic data (diamonds) and inversion response (shaded dots).
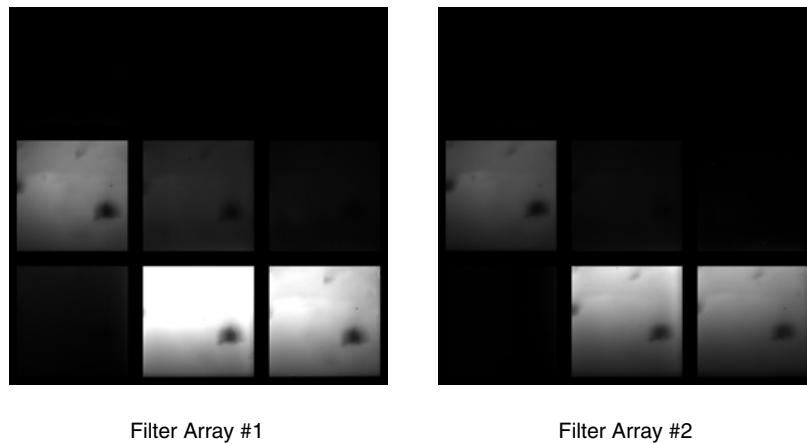
Filter Array #1   Filter Array #2

Figure 8. Ambient light images of Lobo from both ALISS filter arrays. The shortest-wavelength filters are in the upper right-hand corners and the longest-wavelength filters are in the lower left-hand corners. Light intensity appears to increase with increasing wavelength until the longest-wavelength filters (>900 nm) where attenuation becomes dominant. Each tile has a ~15 × 15 cm field of view.

through the forward functional) plotted as open circles in Figure 6a correspond well to the actual ALISS data.

[22] While we know that thermal radiation is occurring at vents, we are also looking for excess light in the visible wavelengths. In order to test the ability of the inversion program to resolve this, a synthetic data set was created. A synthetic light curve (a 330°C blackbody flux with an excess intensity of 10^4 photons $cm^{-2} s^{-1} sr^{-1}$ from 500 to 550 nm (Figure 7a)) was run through the forward functional to generate synthetic data (Figure 7b). The synthetic data were inverted and compared to the original synthetic light curve. The inversion response (shaded dots) fits the synthetic data (open circles) well (Figure 7b). The inversion model is smoother than the synthetic curve but is able to retrieve the excess flux in the 500–550 nm region.

5. Ambient Light Images

5.1. Flanges

[23] ALISS imaged two flange pools (Lobo Flange and Dudley Flange) during the 1998 *Alvin* cruise to the Endeavour Segment of the Juan de Fuca Ridge. The relative stability of flange pools provides an excellent environment in which to image pure hydrothermal fluids that are not subject to turbulence, mixing with ambient seawater, and rapid precipitation of minerals. Many of the possible sources of vent light other than thermal radiation such as chemiluminescence, vapor bubble luminescence, crystalloluminescence, and triboluminescence (described in section 6) are dependent on these processes. Hence it can be postulated that light emission from flange pools is solely due to thermal radiation.

[24] Processed images of Lobo Flange taken with both filter arrays are shown in Figure 8. In each tile the upper portion of the image is brighter than the lower portion. This is due to the oblique orientation of the camera during imaging (see Figure 3). Most of the ambient light is emitted between 700 and 900 nm (at wavelengths longer than 900 nm the attenuation in seawater becomes dominant). Ambient light images from both Lobo and Dudley (Figure 9) show dark features that appear to be sulfide material protruding through the flange pools into cold ambient seawater (as noted by observers on the dive); thus the material does not emit significant thermal light.

[25] As predicted, light from Lobo Flange appears to be purely thermal radiation. The inversion spectrum from Lobo Flange is shown in Figure 10. Only the brightest/closest portion of the

image, ~20 cm^2, was used in the spectral calculation. The temperature of the flange pool was measured to be a steady 332°C with the *Alvin* temperature probe. Because the flange pool is not an ideal blackbody, it has an emissivity of <1; emissivity is the ratio of the thermal radiation of a body to that of an ideal blackbody at the same temperature. The photon flux from Lobo Flange corresponds well to the predicted flux from a 332°C blackbody with an emissivity of 0.9. The high emissivity suggests that the dominant light emission is from the hot rock backing the flange pool rather than the fluid itself; a dark opaque object has a higher emissivity than a semitransparent one. It must be noted that emissivity most likely varies with wavelength, but our analysis is unable to resolve wavelength dependence.

[26] For Dudley Flange, two portions (~11 cm^2) of the image were analyzed, differentiated by the presence or absence of dark features in the ambient images (Figure 9). Inversion spectra from these areas are compared to the spectrum of Lobo Flange in Figure 10. The area without dark features corresponds to the emission from Lobo (i.e., purely thermal radiation). However, the area with dark features shows excess emission in the 500–550 nm region. This excess flux is above the detection level of the camera and cannot be explained by thermal radiation. The mechanism by which solid material protruding through a flange pool leads to visible light emission is not obvious. However, the existence of such material may induce local vertical mixing or
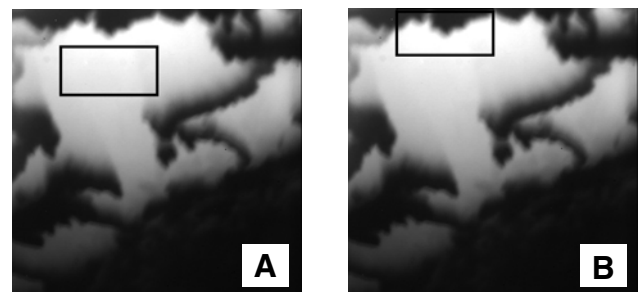

Figure 9. Ambient light images of Dudley Flange from the 870-nm filter (~140 nm in bandwidth). The boxes on the Dudley images indicate areas isolated for spectral analysis: (a) a bright region and (b) a region with dark features. The field of view of each image is ~15 × 15 cm.
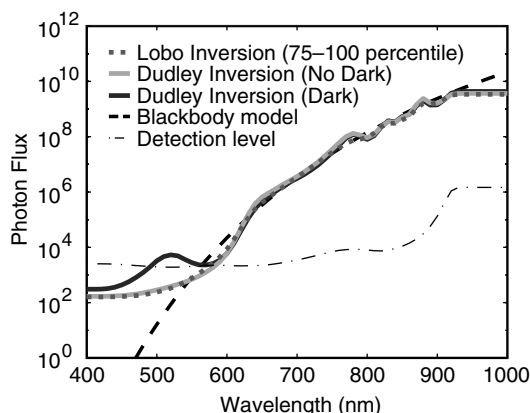
Figure 10. Inversion models for Lobo and Dudley Flanges. Photon fluxes (photons cm^{-2} s^{-1} sr^{-1}) at Lobo (dotted line) and Dudley (shaded line) correspond well to a 332°C blackbody with an emissivity of 0.9. The spectrum from the area of Dudley which includes dark features (dark line) shows excess emission above thermal radiation in the 500–550 nm region that is above the camera detection level.

precipitation on the substrate, which could be associated with nonthermal emission mechanisms.

5.2. Black Smokers

[27] Black smoker vents were imaged at both 9°N on the East Pacific Rise and the Endeavour Segment of the Juan de Fuca Ridge. Vents in both areas (e.g., Peanut Vent in the Main Endeavour Field and Q Vent in the Venture Hydrothermal Field) emitted light that appeared to be purely thermal radiation. However, other vents showed significant emission at some wavelengths above what is expected for thermal radiation alone. Puffer Vent in the Main Endeavour Field was imaged on two dives 3 days apart. On *Alvin* dive 3234, thermal radiation and excess visible light was observed; however, on dive 3237, only thermal radiation was detected. We will show data from four black smoker vents, which emit radiation in the visible region greater than that predicted for thermal radiation alone. These vents fall into two categories: (1) excess narrow-band emission in the 500–600 nm region and (2) excess wideband emission.

5.2.1. Narrow-band emission: Puffer Vent and P Vent.

[28] Puffer Vent (dive 3234) in the Main Endeavour Field and P Vent in the Venture Hydrothermal Field have narrow-band emission in the 500–600 nm range. Puffer Vent appeared to be boiling, and a maximum temperature of 372°C was measured inside the orifice. Unlike most black smokers, where the fluid exits from the top of a chimney-like structure, fluid at Puffer Vent is directed downward from a large sulfide structure and then rises buoyantly (Figure 11a). It is difficult to see the orifice under illuminated conditions due to the smoky fluid; however, ambient light images show clearly where the highest temperature (and hence the orifice) is located (Figure 11b). The ambient light image at Puffer Vent was divided into four regions based on the intensity quartiles (as described in section 4.1) (Figure 11c, inset). Pixels in the highest intensity quartile (75–100 percentile) are clustered around the orifice, while pixels in the lowest intensity quartile (0–25 percentile) are found along the fringes of the source mask (~5 cm from the orifice). The inversion spectra from these regions are plotted in Figure 11c. The highest-intensity quartile has an emission spectrum that resembles a blackbody. The temperature just outside of the orifice (the highest temperature that ALISS can "see") was measured to be

~330°C with the *Alvin* temperature probe. An emissivity of 0.3 is required to match the thermal radiation from a 330°C source to the flux observed at the orifice of Puffer Vent. Indeed, the semitransparent nature of black smoker fluid would suggest a relatively low emissivity as compared to a flange pool backed by hot opaque rock.

[29] Emission spectra from the regions of Puffer Vent away from the orifice correspond to thermal radiation at long wavelengths (>650 nm). The intensity of the thermal emission decreases with increasing distance from the orifice and hence decreasing temperature. At shorter wavelengths, excess light emission is observed in the 500–550 nm region (Figure 11c). This excess emission is >10^4 photons cm^{-2} s^{-1} sr^{-1} in the 50–75 percentile region and decreases to near the detection limit in the 0–25 percentile region. Puffer was imaged 3 days later and showed no excess light emission at that time. Thus nonthermal emission in the visible region can vary with time.

[30] P Vent (Figure 12aa) had a maximum orifice temperature of ~377°C. Its inversion spectra (Figure 12b) are very similar to those of Puffer Vent. The flux at the orifice (75–100 percentile region) corresponds to a 340°C blackbody with an emissivity of 0.3 with no excess emission in the visible region. In the regions
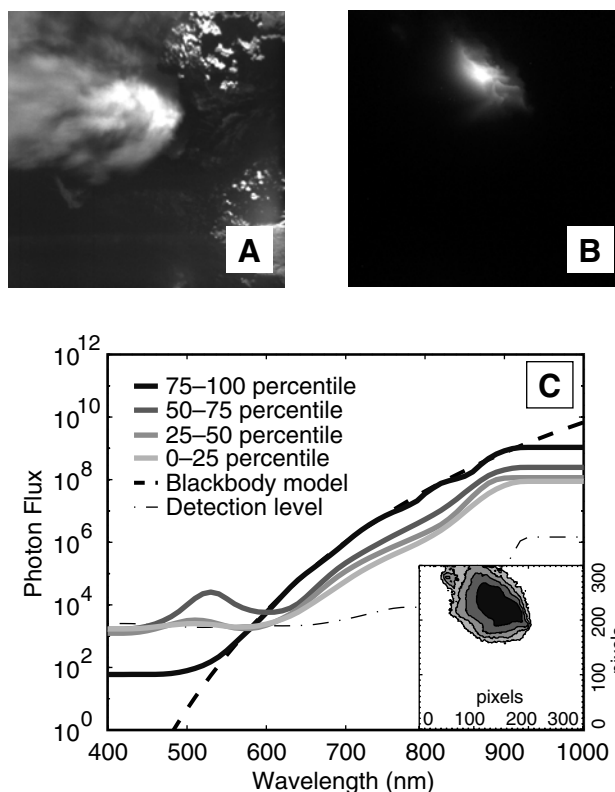

Figure 11. Ambient image and inversion models for Puffer Vent. (a) Image of Puffer Vent from the 550-nm filter illuminated by *Alvin*'s lights. Hydrothermal fluid exists downward before rising buoyantly. The field of view is ~15 × 15 cm. (b) Ambient light image of Puffer Vent from the 870-nm filter. Light is only observed right at the vent orifice where the fluid is the hottest. (c) Inversion models of the photon flux (photons cm^{-2} s^{-1} sr^{-1}) from different quartiles of the source area. The inset shows how the source area (15 × 15 cm field of view) is divided into four regions. The photon flux at the orifice (75–100 percentile region) corresponds well to a 330°C blackbody of emissivity 0.3. In regions away from the orifice, photon flux decreases (as would be expected for decreasing temperature) and excess light is observed in the 500–550 nm band.
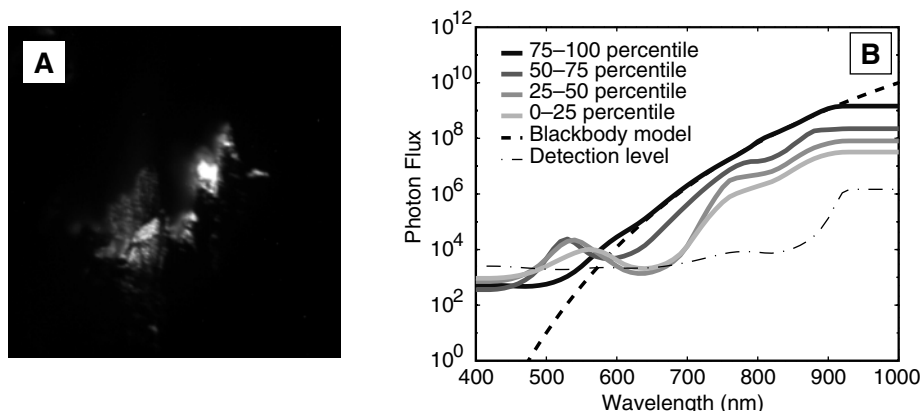
Figure 12. Ambient image and inversion models for P Vent. (a) Ambient light image of P Vent from the 870-nm filter. The field of view is ~15 × 15 cm. (b) Inversion models of the photon flux (photons cm^{-2} s^{-1} sr^{-1}) from different quartiles of the source area. Photon flux at the orifice (75–100 percentile region) corresponds well to a 340°C blackbody of emissivity of 0.3. In regions away from the orifice, photon flux decreases at long wavelengths (as expected for decreasing temperature), and excess light is observed in the 500–600 nm band.

farther away from the orifice, thermal radiation observed at long wavelengths decreases. In the 50–75 and 25–50 percentile regions an excess flux >10^4 photons cm^{-2} s^{-1} sr^{-1} is observed in the 500–550 nm band. The spectrum from the 0–25 percentile region shows a flux of ~10^4 photons cm^{-2} s^{-1} sr^{-1} at 550 nm. These photon fluxes in the visible region of the spectrum must be caused by a source mechanism other than thermal radiation.

5.2.2. Wideband emission: Sully Vent and L Vent.
[31] Sully Vent in the Main Endeavour Field and L Vent in the Venture Hydrothermal Field both emit excess wideband light in the visible region. Sully Vent (Figure 13a) had a maximum orifice temperature of ~373°C and appeared to be boiling. The temperature just outside of the orifice was ~340°C as recorded by the *Alvin* temperature probe. Inversion spectra are shown in Figure 13b. As with previous black smoker vents, emission at long wavelengths is consistent with thermal radiation. Given a maximum temperature of 340°C, an emissivity of 0.3 is required to fit the observed data in the highest quantile region. At shorter

wavelengths (<600 nm), light from the entire source area is on the order of 10^4 photons cm^{-2} s^{-1} sr^{-1}. Light at the orifice (75–100 percentile region) is slightly higher than the lower percentile regions. In addition to the 5-min exposure images, sixty 30-s exposures were also obtained at Sully Vent. The time series obtained from those exposures shows rapid (<30 s) shifts in photon flux in the visible region of the spectrum [*White et al.*, 2000].

[32] L Vent (marker AdV 4–9) in the Venture Hydrothermal Field (Figure 14a) had internal orifice temperature of ~315°C. The inversion spectrum from the orifice (75–100 percentile region) corresponds to a 295°C blackbody with an emissivity of 0.3. Measurements made at L Vent during an April 1996 cruise confirm a temperature of ~295°C at the orifice corresponding to an internal orifice temperature of ~311°C. Like Sully Vent, inversion spectra from L Vent (Figure 14b) correspond to thermal radiation at the long wavelengths (>600 nm) and are on the order of 10^4 photons cm^{-2} s^{-1} sr^{-1} at the short wavelengths (<600 nm). However, unlike Sully Vent, emission at L Vent in the 0–25

Figure 13. Ambient image and inversion models for Sully Vent. (a) Ambient light of image of Sully Vent from the 870-nm filter. The field of view is ~15 × 15 cm. (b) Inversion models of the photon flux (photons cm^{-2} s^{-1} sr^{-1}) from different quartiles of the source area. Long-wavelength photon flux at the orifice (75–100 percentile region) corresponds to thermal radiation from a 340°C body with an emissivity of 0.3. At short wavelengths, photon flux in all quartiles is on the order of 10^4 photons cm^{-2} s^{-1} sr^{-1}.
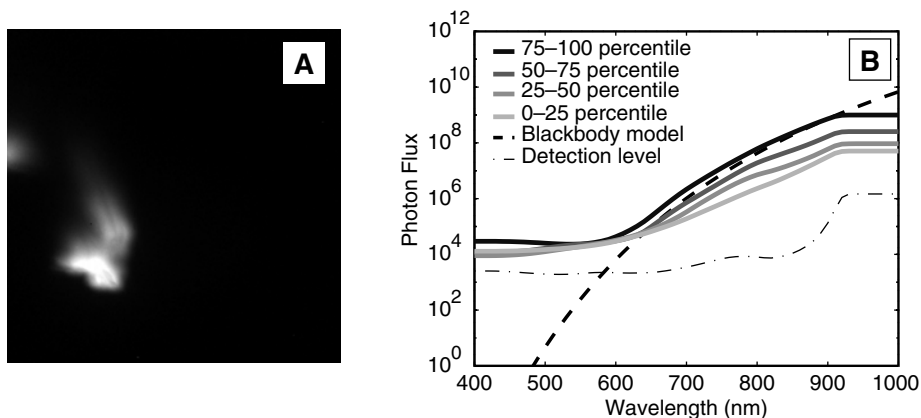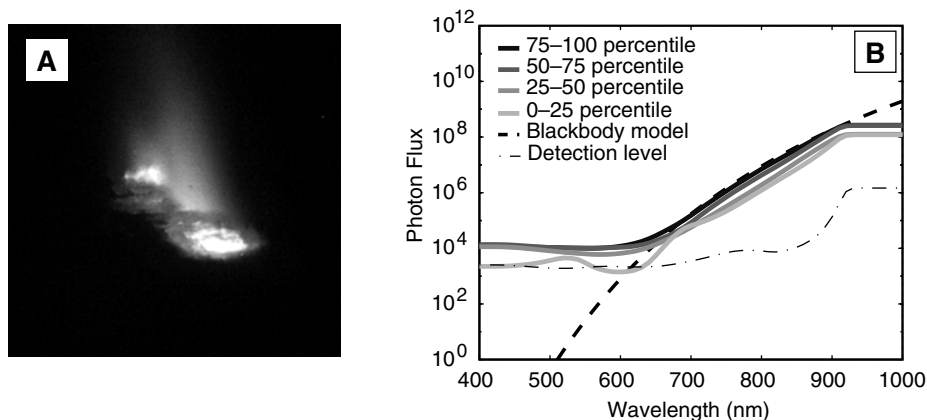
Figure 14. Ambient image and inversion models for L Vent. (a) Ambient light of image of L Vent from the 870-nm filter. The field of view is $\sim$15 $\times$ 15 cm. (b) Inversion models of the photon flux (photons cm^{-2} s^{-1} sr^{-1}) from different quartiles of the source area. Long-wavelength photon flux at the orifice (75–100 percentile region) corresponds to thermal radiation from a 295°C body with an emissivity of 0.3. At short wavelengths, photon flux in the upper quartiles is on the order of 10^4 photons cm^{-2} s^{-1} sr^{-1}. In the 0–25 percentile region the only excess flux observed in the visible band (above the detection level) is between 500 and 600 nm.

percentile region is only above the detection limit in the 500–550 nm band.

5.3. Beehive

[33] One beehive structure was imaged with ALISS at Q Vent in the Venture Hydrothermal Field. The beehive is visible on the left third of the ALISS image (Figure 15a). Sectioning the source area by intensity does not isolate significant portions of the beehive (and the spectra from those regions do not vary significantly). Thus the entire structure was analyzed as one unit ("beehive structure"; Figure 15b). In an effort to analyze pure fluid without rock behind it the area outside of the source region but within 1 or 2 cm of the beehive was isolated ("fluid layer"; Figure 15b).

[34] Inversion spectra from the beehive and the fluid layer are shown in Figure 15b. Photon flux from the beehive corresponds to a 265°C blackbody of emissivity of 0.9 at wavelengths >650 nm. No temperature measurements were made at the beehive. An emissivity of 0.9 was used in the blackbody calculations because

the fluid imaged is backed by hot opaque rock, similar to a flange pool. Assuming the light from the fluid layer is dominated by thermal emission from fluid in contact with the beehive structure (i.e., $\sim$265°C fluid), emissivity of the fluid may be as low as 0.1. This low value of emissivity is not surprising given the low absorptivity of clear water. The spectra from the beehive and the fluid layer both show a photon flux of $\sim$10^4 photon cm^{-2} s^{-1} sr^{-1} in the 600–650 nm region. In the 500–600 nm region the beehive has a flux of 10^4 photons cm^{-2} s^{-1} sr^{-1}, while that of the fluid layer is below the detection level. Comparing light emission from the beehive structure to that from the fluid itself suggests that excess light at 600–650 nm is due to a fluid-related mechanism, such as mixing or turbulence, while the 500–550 nm excess emission observed only at the beehive may be related to mineral-related mechanisms, such as precipitation. The spectrum from the fluid layer shows a dip in emission at 800 nm. While it is not easily seen in the inversion spectrum, ALISS data from the beehive structure indicate a similar dip in the 800-nm channel. This type of decrease in

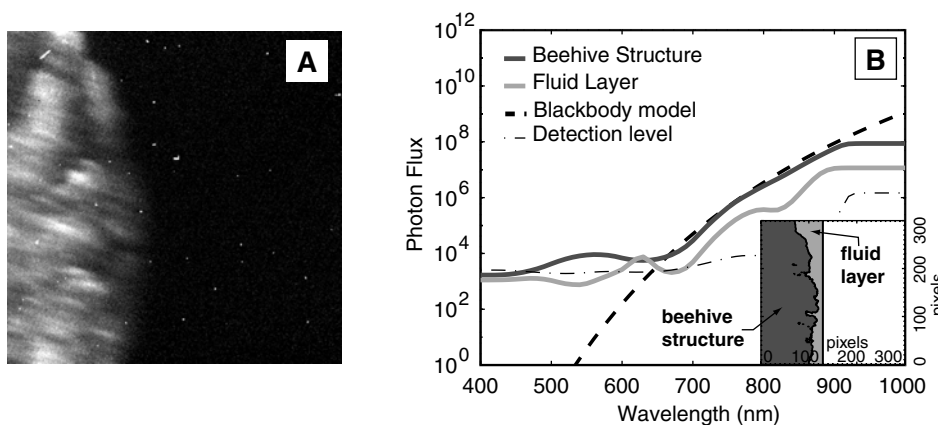**Figure 15.** Ambient image and inversion models for a beehive structure at Q Vent. (a) Ambient light image of the beehive from the 870-nm filter. The beehive structure is in the left third of the image. The field of view is $\sim$15 $\times$ 15 cm. (b) Inversion models of the photon flux (photons cm^{-2} s^{-1} sr^{-1}) from the beehive structure and the fluid layer; the inset shows the regions analyzed.

long-wavelength light was not observed at other vents and cannot be easily explained.

6. Discussion

6.1. Light Emission and Possible Sources

[35] ALISS data show that light is ubiquitous at all types of high-temperature hydrothermal vents (i.e., flange pools, black smokers, and beehives) in the East Pacific and that thermal radiation is the dominant source at wavelengths above 650 nm. This radiation is dependent entirely on the temperature of the fluid and its emissivity. Since flange pools and beehive structures are backed by hot, opaque rock, they are expected to have a higher emissivity than the semitransparent fluid of a black smoker. Emissivity was estimated from ALISS data and recorded vent temperatures by assuming that long-wavelength light emission was purely thermal radiation. Lobo Flange and Dudley Flange both emit light consistent with thermal radiation from a $332°C$ body of emissivity of 0.9. The temperature of black smoker fluid drops by $20-30°C$ on exiting the orifice, and the emissivity appears to be ~ 0.3. Clear hydrothermal fluid (such as that emanating from a beehive) may be as low as 0.1.

[36] Mechanisms other than thermal radiation are also responsible for light emission at hydrothermal vents. A number of these mechanisms are discussed in greater detail by *Reynolds* [1995] and *White* [2000]. *Tapley et al.* [1999] documented chemiluminescence, the direct conversion of chemical energy to light, during sulfide oxidation in seawater. Hydrothermal vent fluids contain significant concentrations of sulfide and undergo rapid mixing with oxygenated seawater entrained in the vent plume, making chemiluminescence a likely source of vent light. Light emission can be associated with both crystallization and fracturing of minerals, crystalloluminescence (XTL) and triboluminescence (TL), respectively. A number of minerals prevalent at hydrothermal vents, within the chimney structure and as precipitates in the plume, such as sphalertie (ZnS) and chalcopyrite (CuFeS$_2$) [*Haymon*, 1983; *Tivey and McDuff*, 1990] are known to be TL and XTL active [*Nelson*, 1926; *Reynolds*, 1995, and references therein; *Walton*, 1977]. *Chakravarty and Walton* [2000] and *Reynolds* [2000] describe a newly identified type of luminescence (vapor bubble luminescence) associated with the condensation of macroscopic vapor bubbles in water, produced by injecting steam into water. Emission is observed both in freshwater and seawater and does not appear to be wavelength dependent in the $380-600$ nm region. Because of the complexity of hydrothermal systems and the lack of detailed information on possible mechanisms, we cannot confirm quantitatively the extent to which any nonthermal source contributes to vent light.

[37] Although flanges were expected to emit purely thermal radiation, nonthermal emission was also observed. Some flanges have solid material protruding through the hot flange pool into cold ambient seawater. This is seen as dark features in the ambient light images (e.g., Figure 9). At Dudley Flange, excess light emission in the $500-550$ nm band is observed in the vicinity of this material. It is possible that precipitation is actively occurring on these features or that they induce local mixing. Analyses of the protruding material may help to determine whether processes such as crystalloluminescence or chemiluminescence are occurring due to those mechanisms.

[38] The ALISS data show three cases of purely thermal radiation at black smokers: Peanut Vent and Puffer Vent (dive 3237) on the Juan de Fuca Ridge and Q Vent at 9°N on the East Pacific Rise. A number of black smoker vents also emit excess light over that predicted for thermal radiation in the visible region of the spectrum (<700 nm). Repeated measurements at Puffer Vent and Sully Vent suggest that the intensity of this light can vary over time [*White et al.*, 2000]. The spatial and spectral data obtained with ALISS can be used to infer which sources are responsible for the nonthermal light. Most nonthermal light is associated with the cooler regions of the plume. This can be seen at Puffer Vent (dive 3234) and P Vent where significant light is observed away from the orifice (0–25, 25–50, and 50–75 percentile regions) at $\sim 500-$ 600 nm. This suggests mechanisms related to mixing (chemiluminescence) or precipitation (crystalloluminescence or triboluminescence) which do not occur directly at the orifice. As hydrothermal fluid exits a vent, it entrains and mixes with oxygenated, ambient ($\sim 2°C$) seawater. This mixing and associated cooling leads to sulfide oxidation and the precipitation of minerals such as sphalerite in the vent plume [e.g., *Baron*, 1998].

[39] In some cases, excess light over thermal radiation is observed at the orifice (75–100 percentile region). At Sully Vent and L Vent, significant light is observed from 450 to 600 nm for the entire source area. These vents do not appear to be different from the other vents in any way (i.e., in chemistry, temperature, size), so their wideband emission is perplexing. The only proposed mechanism known to emit wideband radiation is vapor bubble luminescence. However, this mechanism is most likely to occur away from the orifice where quenching of the exiting fluid occurs. It is possible that the wideband light observed at these vents is due to a combination of sources. Experiments on chimney pieces revealed strong TL/XTL emissions from the inside of chimneys (predominantly chalcopyrite) at 450 nm (C. Z. Radziminski et al., unpublished report, 1997). Thus it is possible that at some vents we are observing the signal from mineral precipitation within the chimney conduit scattered outward. The remaining emission from the 500– 600 nm region could be due to chemiluminescence or precipitation of other minerals.

[40] Only one beehive structure was imaged with ALISS. An attempt was made to analyze light emission from both the structure itself and the fluid emanating from it. A flux of $\sim 10^4$ photons cm^{-2} s^{-1} sr^{-1} was observed from both the sulfide structure and the fluid at 600 nm. This emission may be generated in the fluid layer (and thus superimposed on the structure emission). Because the fluid appears to be clear (i.e., no significant precipitation is observed), chemiluminesence (possibly due to sulfide oxidation) is the most likely source mechanism. ALISS data from the sulfide structure show significant light emission in the 500–600 nm band above that predicted for thermal radiation. This emission could be due to crystalloluminescence from the precipitation of minerals on the beehive structure.

[41] A summary of the ambient light data obtained with ALISS is given in Table 1. The photon fluxes determined from the ALISS measurements are less than those recorded by the OPUS instrument [*Van Dover et al.*, 1996]. OPUS was only capable of measuring count rates for each filter. However, as discussed above, the interference filters used by both ALISS and OPUS allowed light leakage outside of the passband. Thus, without inverting the data (as was done with the ALISS measurements), accurate photon fluxes at the vent could not be obtained with OPUS.

6.2. Biological Implications

[42] Hydrothermal vents are home to unique biological communities whose primary producers are chemosynthetic bacteria that extract energy from vent chemicals rather than sunlight [*Jannasch*, 1995]. These bacteria live symbiotically with more complex organisms such as tube worms or are free living and grazed upon by heterotrophic organisms [*Hessler and Kaharl*, 1995; *Van Dover*, 2000]. Because of the depths at which these communities live (thousands of meters below the sea surface) their environments were originally thought to be devoid of significant light. Hence it was not surprising to scientists to find that some shrimp (e.g., *Rimicaris exoculata*) lacked conventional eyes and eyestalks [*Williams and Rona*, 1986]. We now know that significant nonsolar light does exist at hydrothermal vents in the deep ocean and that the supposedly blind shrimp have unique

Table 1. Ambient Light Summary

Vent	Temperature, °C	Photon Flux, photons cm^{-2}s^{-1}sr^{-1}			
		600–700 nm	700–800 nm	800–900 nm	900–1000 nm[a]
Flange Pools					
Lobo	332	6.3×10^6	3.3×10^8	6.1×10^9	$\sim 8.3 \times 10^{10}$
Dudley	332	8.0×10^6	4.9×10^8	7.8×10^9	$\sim 8.3 \times 10^{10}$
Black Smokers					
Puffer	372	1.6×10^6	7.8×10^7	2.1×10^9	$\sim 2.5 \times 10^{10}$
P Vent	377	3.6×10^6	1.6×10^8	3.6×10^9	$\sim 3.8 \times 10^{10}$
Sully	373	4.0×10^6	1.6×10^8	2.5×10^9	$\sim 2.5 \times 10^{10}$
L Vent	315	3.7×10^5	1.6×10^7	4.6×10^8	$\sim 6.9 \times 10^9$

[a] Photon fluxes in the 900–1000 nm region were estimated from blackbody curves fit by the data due to artificial flattening of the inversion models.

nonimaging photoreceptors capable of detecting low levels of light [*O'Neill et al.*, 1995; *Van Dover et al.*, 1989]. The question must now be asked: How does vent light affect surrounding biological communities?

[43] Are vent animals capable of seeing vent light, and if so, how do they use this information? As discussed in section 1, the vent shrimp *Rimicaris exoculata* has developed a dorsal photoreceptor uniquely designed to detect low light levels [*O'Neill et al.*, 1995]. Two other Mid-Atlantic vent shrimp (*Chorocaris chacei* and *Mirocaris fortunata*) were found to have similar photoreceptive organs [*Van Dover*, 2000, and references therein]. No comparable photosensitive macroorganisms have been found in the East Pacific where the present data were obtained. Calculations by *Pelli and Chamberlain* [1989] suggest that the photoreceptors of *R. exoculata* are capable of detecting a 350°C vent; however, they note that only behavioral evidence can prove that the shrimp actually see vent light. If *R. exoculata* does see vent light, it may have either positive or negative phototactic responses: being able to see vents may lead the shrimp to food (i.e., the chemosynthetic bacteria prevalent at vents), or away from vent fluid hot enough to cook them [*Van Dover*, 2000].

[44] A more challenging (and controversial) question is: Does photosynthesis occur at deep-sea hydrothermal vents? A number of phototrophic organisms are adapted to live in low-light conditions. These include organisms living at the bottom of the pelagic photic zone, in shallow benthic environments, and beneath polar ice. Bacteria appear to adapt well to low-light conditions. Five strains of a photosynthetic, brown, sulfur bacterium (*Chlorobium phaeobacteriodes*) have been isolated from a depth of 80 m in the Black Sea [*Overmann et al.*, 1992]. All strains were found to be extremely low-light adapted, thriving at light intensities <6 × 10^{13} photons cm^{-2} s^{-1}. In fact, the amount of light reaching 80 m depth was calculated to be on the order of 10^{11} photons cm^{-2} s^{-1}. Species of green bacteria (e.g., genera *Pelodictyon* and *Ancalochloris*) and purple bacteria are also able to survive at low light levels ($\sim 6 \times 10^{13}$ photons cm^{-2} s^{-1}) and low sulfide concentrations [*Pfennig*, 1978]. However, even these extremely low-light levels are well above the levels observed at deep-sea vents.

[45] For an organism to be able to photosynthesize using vent light it must contain pigments that absorb at long wavelengths (where light emission is strongest), and it would have to live close to the vent fluid where attenuation effects are minimal. However, attenuation of light in seawater is strong at long wavelengths (~ 0.2 cm^{-1} at 950 nm). At a distance of 3.5 cm from the flange the intensity drops by half. At 11.5 cm away the intensity is reduced to one tenth of that at the flange pool. Thus the possibility of hydrothermally driven photosynthesis is marginal, and, at present, no known phototrophs have been identified at deep-sea vents [*Kolber et al.*, 2000; *Yurkov and Beatty*, 1998]. While obligate photosynthesis is unlikely at deep-sea vents,

facultative photosynthesis and photoheterotrophy cannot yet be ruled out.

References

Baron, S. R., Hydrothermal vent precipitates: A study of temporal and geographic variations in black smoker particles and chimneys from 9–10°N, East Pacific Rise, Doctoral thesis, Univ. of Calif., Santa Barbara, 1998.

Behr, B., CCD quantum efficiency test (QETest) system v1.0 user's manual, Calif. Inst. of Technol., Palomar CCD Lab., Palomar, 1996.

Belcher, E. H., The luminescence of irradiated transparent media and the Cerenkov effect, I, The luminescence of aqueous solutions of radioactive isotopes, *Proc. R. Soc. London, Ser. A*, *216*, 90–102, 1953.

Bradner, H., et al., Bioluminescence profile in the deep Pacific Ocean, *Deep Sea Res.*, *34*, 1831–1840, 1987.

Chakravarty, A., and A. J. Walton, Light emission from collapsing superheated steam bubbles in water, *J. Lumin.*, *92*, 27–33, 2000.

Constable, S. C., R. L. Parker, and C. G. Constable, Occam's inversion: A practical algorithm for generating smooth models from electromagnetic sounding data, *Geophysics*, *52*(3), 289–300, 1987.

Crane, K., F. Aikman, R. Embley, S. Hammond, A. Malahoff, and J. Lupton, The distribution of geothermal fields on the Juan de Fuca Ridge, *J. Geophys. Res.*, *90*(B1), 727–744, 1985.

Curcio, J. A., and C. C. Petty, The near infrared absorption spectrum of liquid water, *J. Opt. Soc. Am.*, *41*, 302–304, 1951.

Delaney, J. R., V. Robigou, R. E. McDuff, and M. K. Tivey, Geology of a vigorous hydrothermal system on the Endeavour Segment, Juan de Fuca Ridge, *J. Geophys. Res.*, *97*(B13), 19,663–19,682, 1992.

Franklin, J., Well-posed stochastic extensions of ill-posed linear problems, *J. Math. Anal. Appl.*, *31*, 682–716, 1970.

Hale, G. M., and M. R. Querry, Optical constants of water in the 200-nm to 200-mm wavelength region, *Appl. Opt.*, *12*, 555–563, 1973.

Haymon, R. M., Growth history of hydrothermal black smoker chimneys, *Nature*, *301*, 694–698, 1983.

Haymon, R. M., D. J. Fornari, M. H. Edwards, S. Carbotte, D. Wright, and K. C. Macdonald, Hydrothermal vent distribution along the East Pacific Rise crest (9°09′–54′N) and its relationship to magmatic and tectonic processes on fast-spreading mid-ocean ridges, *Earth Planet. Sci. Lett.*, *104*, 513–534, 1991.

Hessler, R. R., and V. A. Kaharl, The deep-sea hydrothermal vent community, in *Seafloor Hydrothermal Systems: Physical, Chemical, Biological, and Geological Interactions*, *Geophys. Monogr. Ser.*, vol. 91, edited by S. E. Humphris et al., pp. 72–84, AGU, Washington, D. C., 1995.

Jannasch, H., Microbial interactions with hydrothermal fluids, in *Seafloor Hydrothermal Systems: Physical, Chemical, Biological, and Geological*

Interactions, Geophys. Monogr. Ser., vol. 91, edited by S. E. Humphris et al., pp. 273–296, AGU, Washington, D. C., 1995.

Jerlov, N. G., *Optical Oceanography*, 194 pp., Elsevier Sci., New York,1968.

Kolber, Z. S., C. L. Van Dover, R. A. Niederman, and P. G. Falkowski, Bacterial photosynthesis in surface waters of the open ocean, *Nature*, *407*, 177–179, 2000.

Kou, L., D. Labrie, and P. Chylek, Refractive indices of water and ice in the 0.65 to 2.5mm spectral range, *Appl. Opt.*, *32*, 3531–3540, 1993.

Nelson, D. M., Photographic spectra of tribo-luminescence, *J. Opt. Soc. Am.*, *12*, 207–215, 1926.

O'Neill, P. J., R. N. Jinks, E. D. Herzog, B.-A. Battelle, L. Kass, G. H. Renninger, and S. C. Chamberlain, The morphology of the dorsal eye of the hydrothermal vent shrimp, *Rimicaris exoculata*, *Visual Neurosci.*, *12*, 861–875, 1995.

Overmann, J., H. Cypiowka, and N. Phennig, An extremely low-light-adapted phototrophic sulfur bacteria from the Black Sea, *Limnol. Oceanogr.*, *370*, 150–155, 1992.

Pegau, W. S., D. Grey, and J. R. Zaneveld, Absorption and attenuation of visible and near-infrared light in water: dependence on temperature and salinity, *Appl. Opt.*, *36*, 6035–6046, 1997.

Pelli, D. G., and S. C. Chamberlain, The visibility of 350°C blackbody radiation by the shrimp *Rimicaris exoculata* and man, *Nature*, *337*, 460–461, 1989.

Pfennig, N., General physiology and ecology of photosynthetic bacteria, in *The Photosynthetic Bacteria*, edited by R. K. Clayton, and W. R. Sistrom, pp. 3–18, Plenum, New York, 1978.

Pope, D. G., and E. S. Fry, Absorption spectrum (380–700 nm) of pure water, II, Integrating cavity measurements, *Appl. Opt.*, *36*, 8710–8723, 1997.

Reynolds, G. T., Light and life at hydrothermal vents, *Tech. Rep. 6*, 19 pp., Princeton Univ., Princeton, N. J., 1995.

Reynolds, G. T., Evidence for vapor bubble luminescence, *Tech. Rep. 1*, 6 pp., Princeton Univ., Princeton, N. J., 2000.

Roberts, A., Potassium 40 in the ocean and how to live with it, in *DUMAND 78*, edited by A. Roberts, pp. 139–148, Univ. of Hawaii, Honolulu, 1979.

Smith, J. T., and J. R. Booker, Magnetotelluric inversion for minimum structure, *Geophysics*, *53*, 1565–1576, 1988.

Smith, M. O., and J. R. Delaney, Variability of emitted radiation from two hydrothermal vents, *Eos Trans. AGU*, *70*, 1161, 1989.

Smith, R. C., and K. S. Baker, Optical properties of the clearest natural waters (200–800 nm), *Appl. Opt.*, *20*, 177–184, 1981.

Sullivan, S. A. , Experimental study of the absorption in distilled water, artificial sea water, and heavy water in the visible region of the spectrum, *J. Opt. Soc. Am.*, *53*, 962–968, 1963.

Tapley, D. W., G. R. Buettner, and J. M. Shick, Free radical and chemiluminescence as products of the spontaneous oxidation of sulfide in seawater, and their biological implications, *Biol. Bull.*, *196*, 52–56, 1999.

Tikhonov, A. V., On solution of ill-posed problems, *Dokl. Akad. Nauk*, *151*, 501–504, 1963.

Tikhonov, A. V., On regularization of ill-posed problems, *Dokl. Akad. Nauk*, *153*, 49–52, 1963.

Tivey, M. K., Modeling chimney growth and associated fluid flow at seafloor hydrothermal vent sites, in *Seafloor Hydrothermal Systems: Physical, Chemical, Biological, and Geological Interactions*, Geophys. Monogr. Ser., vol. 91, edited by S. E. Humphris et al., pp. 158–177, AGU, Washington, D. C., 1995.

Tivey, M. K., and J. R. Delaney, Growth of large sulfide structures on the Endeavour Segment of the Juan de Fuca Ridge, *Earth Planet. Sci. Lett.*, *77*, 303–317, 1986.

Tivey, M. K., and R. E. McDuff, Mineral precipitation in the walls of black smoker chimneys: a quantitative model of transport and chemical reactions, *J. Geophys. Res.*, *95*(B8), 12,617–12,637, 1990.

Tyson, J. A., Low-light-level charge-coupled device imaging in astronomy, *J. Opt. Soc. Am.*, *3*, 2131–2138, 1986.

Tyson, J. A., Progress in low-light-level charge-coupled device imaging in astronomy, *J. Opt. Soc. Am.*, *7*, 1231–1236, 1990.

Van Dover, C. L., *The Ecology of Deep-Sea Hydrothermal Vents*, 424 pp., Princeton Univ. Press, Princeton, N. J., 2000.

Van Dover, C. L., E. Z. Szuts, S. C. Chamberlain, and J. R. Cann, A novel eye in "eyeless" shrimp from hydrothermal vents of the Mid-Atlantic Ridge, *Nature*, *337*, 458–460, 1989.

Van Dover, C. L., J. R. Cann, C. Cavanaugh, S. C. Chamberlain, J. R. Delaney, D. Janecky, J. Imhoff, J. A. Tyson, and L. W. Participants, Light at deep sea hydrothermal vents, *Eos Trans. AGU*, *75*, 44–45, 1994.

Van Dover, C. L., G. T. Reynolds, A. D. Chave, and J. A. Tyson, Light at deep-sea hydrothermal vents, *Geophys. Res. Lett.*, *23*(16), 2049–2052, 1996.

Walton, A. J., Triboluminescence, *Adv. Phys.*, *26*, 887–948, 1977.

White, S. N., An investigation into the characteristics and sources of light emission at deep-sea hydrothermal vents, Doctoral thesis, MIT/WHOI Joint Program, Woods Hole, Mass., 2000.

White, S. N., A. D. Chave, J. W. Bailey, C. L. Van Dover, and G. T. Reynolds, Measurements of light at hydrothermal vents, 9° N East Pacific Rise, *Eos Trans. AGU*, *77*(46), Fall Meet. Suppl., F404, 1996.

White, S. N., A. D. Chave, G. T. Reynolds, E. J. Gaidos, J. A. Tyson, and C. L. Van Dover, Variations in ambient light emission from black smokers and flange pools on the Juan de Fuca Ridge, *Geophys. Res. Lett.*, *27*(8), 1151–1154, 2000.

Williams, A. B., and P. A. Rona, Two new caridean shrimps (Bresiliidae) from a hydrothermal field on the Mid-Atlantic Ridge, *J. Crust. Biol.*, *6*, 446–462, 1986.

Yurkov, V., and J. T. Beatty, Isolation of aerobic anoxygenic photosynthetic bacteria from black smoker plume waters of the Juan de Fuca Ridge in the Pacific Ocean, *Appl. Environ. Microbiol.*, *64*, 337–341, 1998.

————————

A. D. Chave and S. N. White, Department of Applied Ocean Physics and Engineering, Woods Hole Oceanographic Institution, Woods Hole, MA 02543, USA. (achave@whoi.edu; snwhite@whoi.edu)

G. T. Reynolds, Department of Physics, Princeton University, Princeton, NJ 08544, USA.